Research Article

Ruonan Fan, Jingting Liu*, Xinzheng Yang, Songying Chen, Deyu Luan*, and Guanlong Lu

Numerical study on flue gas–liquid flow with side-entering mixing

https://doi.org/10.1515/phys-2022-0065
received January 24, 2022; accepted June 28, 2022

Abstract: In this article, the side-entry agitator commonly used in the wet desulfurization absorption tower of a 300 MW thermal power unit was taken as the research object, and the gas–liquid two-phase flow field in the stirring tank was numerically simulated by using the two-fluid model based on Euler–Euler method. The vertical and horizontal velocity field distribution and gas phase distribution in the stirring tank were studied. The results showed that the side-entry agitator formed a "fountain" circulating flow in the stirring tank. The high-speed region of the liquid flow was mainly concentrated near the mixing blade and the bottom banded region. The range of large changes in the fluid velocity was mainly concentrated from the bottom of the mixing tank to 2–3 m from the bottom. The distribution of the oxidizing air was concentrated in the middle of the stirring tank. The mixing effect of two phases in the stirred tank was good, and the oxidizing air was fully diffused. The numerical study in this article has reference significance for in-depth understanding of the flow field and mixing effect of the side-entry agitator.

Keywords: side-entry mixing, two-phase flow, flue gas desulfurization, numerical simulation

1 Introduction

The rapid development of the electric power industry has also brought about problems such as environmental pollution. Thermal power plants have always been a major emitter of greenhouse gases [1], especially the emission of SO_2 has caused a bad impact on the atmospheric environment. In order to effectively control the emission of air pollutants in the thermal power industry, China has carried out ultra-low emission transformation for the thermal power industry, among which the desulfurization of thermal power plants has become the key to control air pollution [2]. Limestone wet flue gas desulfurization is a relatively mature and widely used desulfurization technology [3,4]. The limestone slurry is used for countercurrent washing of the flue gas in the absorption tower to absorb sulfur dioxide in the flue gas, and undergo a series of reactions and dehydration treatments. A powdery gypsum with water content of about 10% is produced. In the absorption tower, the side-entry agitator located in the slurry tank is an important component to maintain the normal operation of the wet flue gas desulfurization system, and it is also the most commonly used stirring method [5]. It has the functions of precipitation, strengthening oxidation air diffusion, and limestone dissolution.

The side-entry agitator of the absorption tower is a kind of mechanical agitation. The liquid is propelled by the stirring blades to generate three basic flows: axial flow, swirling flow, and turbulent flow. Decompose these three flows into an axial part (axial flow) and a non-axial part (rotational or helical flow), as shown in Figure 1. The spiral high-speed axial flow enables the liquid in the low-speed flow area to be carried into the high-speed liquid flow area, so as to play a mixing role, and the non-axial flow formed by the normal thrust will cause the liquid to

* **Corresponding author: Jingting Liu,** School of Mechanical Engineering, Shandong University, Jinan 250061, China; Key Laboratory of High Efficiency and Clean Mechanical Manufacture, Ministry of Education, Shandong University, Jinan 250061, China; National Demonstration Center for Experimental Mechanical Engineering Education, Shandong University, Jinan 250061, China, e-mail: liujingting@sdu.edu.cn
* **Corresponding author: Deyu Luan,** College of Electromechanical Engineering, Qingdao University of Science & Technology, Qingdao 266061, China, e-mail: qddy05@163.com
Ruonan Fan: School of Mechanical Engineering, Shandong University, Jinan 250061, China
Xinzheng Yang: Binzhou Special Equipment Inspection & Research Institute, Binzhou 256600, China
Songying Chen: School of Mechanical Engineering, Shandong University, Jinan 250061, China; Key Laboratory of High Efficiency and Clean Mechanical Manufacture, Ministry of Education, Shandong University, Jinan 250061, China; National Demonstration Center for Experimental Mechanical Engineering Education, Shandong University, Jinan 250061, China
Guanlong Lu: College of Electromechanical Engineering, Qingdao University of Science & Technology, Qingdao 266061, China

Open Access. © 2022 Ruonan Fan *et al.*, published by De Gruyter. This work is licensed under the Creative Commons Attribution 4.0 International License.

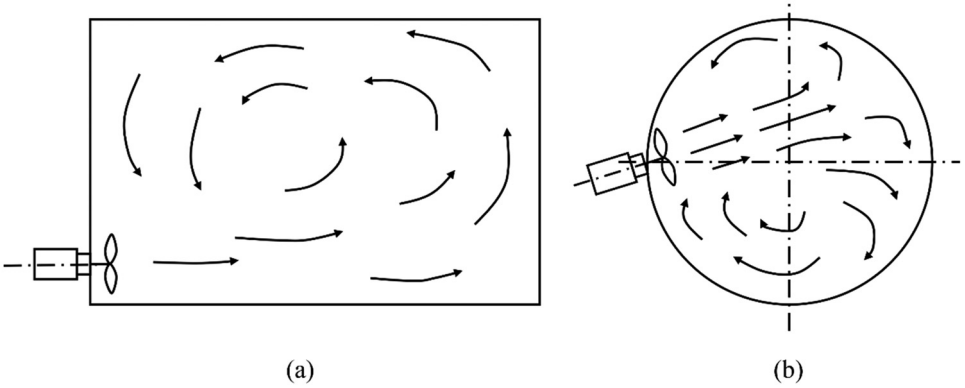

Figure 1: Flow curve of sideway agitator fluid [6]. (a) Non-axial flow (rotating or helical flow); (b) axial flow.

swell up and down, so that the slurry pool can achieve uniform mixing and prevent the accumulation of sediment at the bottom of the tank.

The stirring performance and flow characteristics of side-entering agitators have been studied by some researchers. For the study of two-phase flow, many scholars use computational fluid dynamics (CFD) method for numerical simulation to explore the characteristics of internal two-phase flow field. Gómez *et al.* [7] investigated the flow in a reduced size rectangular tank equipped with a side-entering axial flow impeller in the laminar regime ($18 \leq \mathrm{Re} \leq 120$) by using particle image velocity and CFD. Havryliv *et al.* [8] used the Ansys Fluent 17.0 to model and simulate the mixing process in an industrial-scale vessel with a side-entering agitator. The results showed that mesh size and time step size played a key role for transient CFD simulation and it was very important to find these proper values. Fathonah *et al.* [9] studied the hydrodynamics in side-entering stirring tanks with similar geometric ratio using CFD methods and evaluated the effect of the constant propeller rotational speed and constant tip speed on the pumping capacity and fluid velocity profile in the discharge stream area as well as the flow pattern in the whole tank. Fathonah *et al.* [10] studied the effect of stirred entry angle on the hydrodynamic characteristics in an agitated tank with side-entering mixing tank using the CFD simulation method. The results showed that the average velocity in the tank tended to increase as the stirred entry angle increased. In addition, Al-Kouz *et al.* [11] analyzed the magneto two-phase nanofluid flowing in double wavy enclosure comprehending an adiabatic rotating cylinder by Galerkin finite element. Manzoor *et al.* [12] studied the drag reduction on a square rod detached with two control rods at various gap spacing *via* Lattice Boltzmann Method. For the experimental study on two-phase flow of side-entry agitator, Kehn [13] compared the top-entering *versus* side-entering agitator performance in low viscosity blending by quantifying their power requirements of reaching the same mixing time. Grenville *et al.* [14] measured blend times in a vessel agitated by side-entering agitators using the experimental technique developed by Wesselingh [15] to compare the performance of four common commercially available agitators. Most of the above literatures study the flow field of the stirring tank equipped with a single side-entering agitator, and there are relatively few studies on the internal flow field of the side-entering agitator of the flue gas desulfurization tower.

In order to further study the flow characteristics of the internal flow field of the side-entry agitator, numerical simulation of the flow field in the stirring tank with side-entry agitator was carried out, and the internal flow field velocity distribution and gas phase distribution were analyzed.

2 Numerical simulation method of side-entering agitator

2.1 Simulation working condition of side-entering stirring device

The numerical calculation model in this article was simplified from the actual structure size of the slurry pool at the bottom of the absorption tower for wet desulfurization of 300 MW thermal power unit, as shown in Figure 2. The stirring tank had a flat bottom with a diameter of $T = 11.63$ m and a liquid level of $H = 8.79$ m. At the bottom of the stirring tank, four side-entry agitators were evenly arranged along the circumference of the tank. The agitator blades were installed in the slurry pool of stirring tank, and the stirring shaft formed a certain inclination

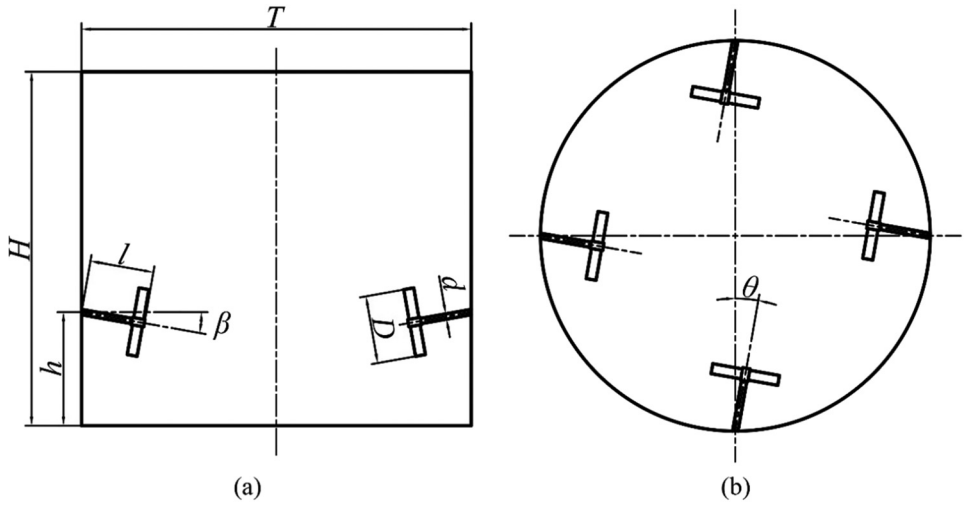

Figure 2: Structure diagram of mixing tank [16]. (a) Main view; (b) top view.

angle with the horizontal line and the center line of the tank, respectively, which is marked as $\beta = 10°$ and $\theta = 7°$.

The paddle type is a four narrow blade detachable rotary paddle agitator [17], as shown in Figure 3. The agitator consists of four blades spaced 90° apart. In order to enhance its axial flow performance, the blade placement angle was $\beta = 45°$. The diameter of the paddle is $D = 1$ m, the width of the paddle is $W = 0.2$ m, and the thickness of the paddle is $\delta = 0.012$ m. The ratio of tank diameter to paddle diameter is $T{:}D \approx 9{:}1$. The stirring shaft diameter is $d = 0.1$ m, and the extension length is $l = 0.8$ m. The lateral installation height of the agitator is $h = 1.41$ m and the speed of the agitator paddle is 194 rpm. The stirring effect requires that when one agitator is not working, the inlet of the pump cannot be blocked, the oxidized air diffuses evenly, and the slurry is stirred evenly and suspended far from the bottom of the tank. The stirring slurry is limestone slurry with a suspended solid volume fraction of 15%, density of $\rho = 1{,}150\ \text{kg/m}^3$, viscosity of $\mu = 2 \times 10^{-3}$ Pa s, particle diameter of 4×10^{-5} m, and pH between −5 and −6.

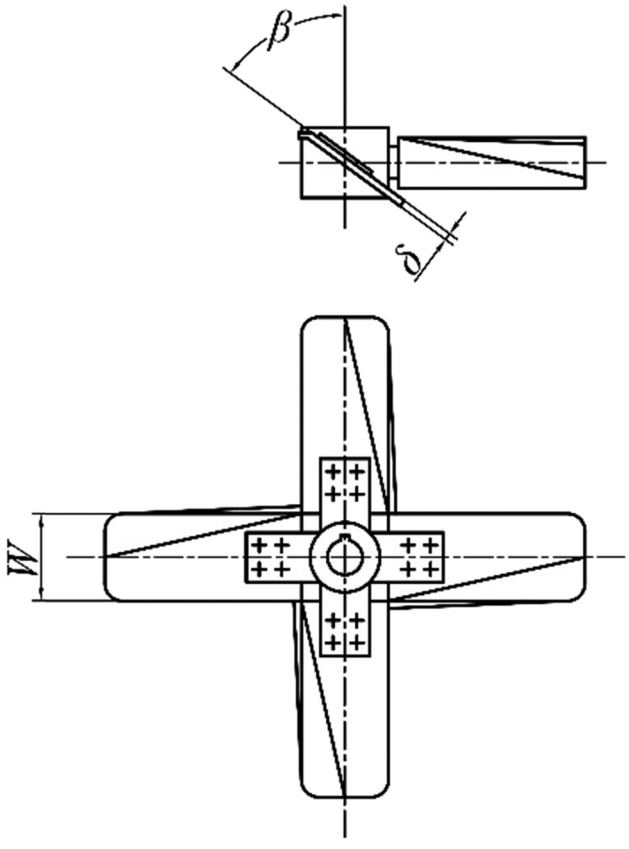

Figure 3: Structure of four narrow blade detachable rotary paddle agitator.

2.2 Governing equation of side-entering stirring device

In this article, a two-fluid model based on Euler–Euler method was used to simulate the gas–liquid two-phase flow field in stirring tank. The Euler–Euler method regards the dispersed phase and fluid such as bubbles and particles as continuous medium. The dispersed phase and the continuous phase coexist and penetrate each other. Both phases are processed in the Euler coordinate system, so they have the same form of governing equations. This model requires less calculation and is the main simulation method for multiphase systems at present [18–20]. The basic equations of the model mainly include the continuity

equation and the momentum conservation equation. This article focused on the flow characteristics in the stirring tank, so the temperature change of gas–liquid two-phase flow is not considered. The governing equation of the model is as follows:

The continuity equation [21,22]:

$$\frac{\partial}{\partial t}(\rho_k \alpha_k) + \nabla \cdot (\rho_k \alpha_k \overrightarrow{u_k}) = 0, \tag{1}$$

where ρ_k, α_k, and $\overrightarrow{u_k}$ are the phase density (kg/m^3), phase fraction, and phase average velocity (m/s), respectively. The subscript k indicates the liquid phase (l) or gas phase (g).

The momentum equation:

$$\frac{\partial}{\partial t}(\rho_k \alpha_k \overrightarrow{u_k}) + \nabla \cdot (\rho_k \alpha_k \overrightarrow{u_k} \overrightarrow{u_k}) = -\alpha_k \nabla p + \nabla \cdot \overline{\overline{\tau}}_{\text{eff},k} + \overrightarrow{R_k} + \overrightarrow{F_k} + \rho_k \alpha_k \overrightarrow{g}, \tag{2}$$

where p is the pressure acting on the two phases, $\tau_{\text{eff},k}$ is the Reynolds stress under the average velocity gradient, R_k is the momentum exchange term, and the interphase momentum exchange is mainly due to the action of the interphase force, which includes drag force, additional mass force, *etc*. F_k is the volume force.

The main purpose of using the gas and liquid turbulence models is to solve the turbulent viscosity, and then obtain the effective viscosity of the fluid in the two-fluid model, so that the two-fluid model is closed. Generally, the k–ε turbulent model is used to calculate the continuous-phase turbulent viscosity [23]. The standard k–ε two-equation turbulence model is a model close to the steady state of turbulent flow in the Reynolds time-averaged method of turbulence calculation method. Considering the calculation cost and calculation accuracy, the standard k–ε turbulence model was used in this article [24], the transport equation of turbulent kinetic energy k and dissipation rate ε of turbulent kinetic energy is:

$$\frac{\partial(\rho k)}{\partial t} + \frac{\partial(\rho k u_i)}{\partial x_i} = \frac{\partial}{\partial x_j}\left[\left(\mu + \frac{\mu_t}{\sigma_k}\right)\frac{\partial k}{\partial x_j}\right] + G_k + G_b - \rho\varepsilon - Y_M + S_k, \tag{3}$$

$$\frac{\partial(\rho \varepsilon)}{\partial t} + \frac{\partial(\rho \varepsilon u_i)}{\partial x_i} = \frac{\partial}{\partial x_j}\left[\left(\mu + \frac{\mu_t}{\sigma_\varepsilon}\right)\frac{\partial \varepsilon}{\partial x_j}\right] + C_{1\varepsilon}\frac{\varepsilon}{k}(G_k + C_{3\varepsilon}G_b) - C_{2\varepsilon}\rho\frac{\varepsilon^2}{k} + S_\varepsilon, \tag{4}$$

where u_i denotes the component of fluid velocity along i direction, k denotes the turbulent kinetic energy, ε denotes the turbulent dissipation rate, μ_t is the turbulent viscosity coefficient, and $\mu_t = \rho C_\mu \frac{k^2}{\varepsilon}$, C_μ is the empirical constant. G_k denotes the turbulent kinetic energy generated by laminar velocity gradient, G_b denotes the turbulent kinetic energy generated by buoyancy, Y_M denotes the contribution of fluctuating expansion to the total dissipation rate in compressible turbulence, σ_k and σ_ε are the Prandtl numbers corresponding to the turbulent kinetic energy and dissipation rate, respectively. S_ε and S_k are user-defined, $C_{1\varepsilon}$, $C_{2\varepsilon}$, and $C_{3\varepsilon}$ are empirical constant. In the standard k–ε turbulence model, the value of each model constant is $C_{1\varepsilon} = 1.44$, $C_{2\varepsilon} = 1.92$, $C_\mu = 0.09$, $\sigma_k = 1.0$, and $\sigma_\varepsilon = 1.3$, according to the recommended value of Launder and Spalding [25] and subsequent experimental verification.

2.3 Computing domain and grid division

Due to the geometric symmetry of the stirring tank, a quarter of the stirring tank was selected as the computational domain in order to simplify the calculation. For the side-entering stirring device, the computational domain was divided into two parts, as shown in Figure 4(a), due to the existence of rotating dynamic boundary and stationary static boundary. One part (a) contained the moving blades and the other part (b) contained the stationary baffle and tank. Two reference frames were used for the calculation of two regions. The rotating reference frame was used in the area where the blades were located, and the stationary reference frame was used for the other part. At the interface of two reference frames, the flow was assumed to be steady, *i.e.*, the velocity at the interface must be the same for both reference frames. However, the cell node was static throughout the calculation. When using the above method to divide the dynamic and static areas, it must be ensured that the normal velocity of the nodes on the interface is zero, *i.e.*, the top view of the interface must be circular rather than quadrilateral or other shapes.

In this article, the pre-processing software Gambit was used to generate grids. The computational domain was large and irregular, so the method of combining structured and unstructured grid was used to divide the grid into blocks, and the computational domain was divided into three parts: the rotating part of blades, the stationary region at the bottom of the stirring tank, and the stationary region at the upper part of the stirring tank. The stationary region at the upper part of the stirring tank was regular in shape, so the structured grid was divided by hexahedral mesh. The structure of the blade rotation area and the static area at the bottom of the stirring tank was more complex, so the adaptable tetrahedral unstructured mesh was used to divide

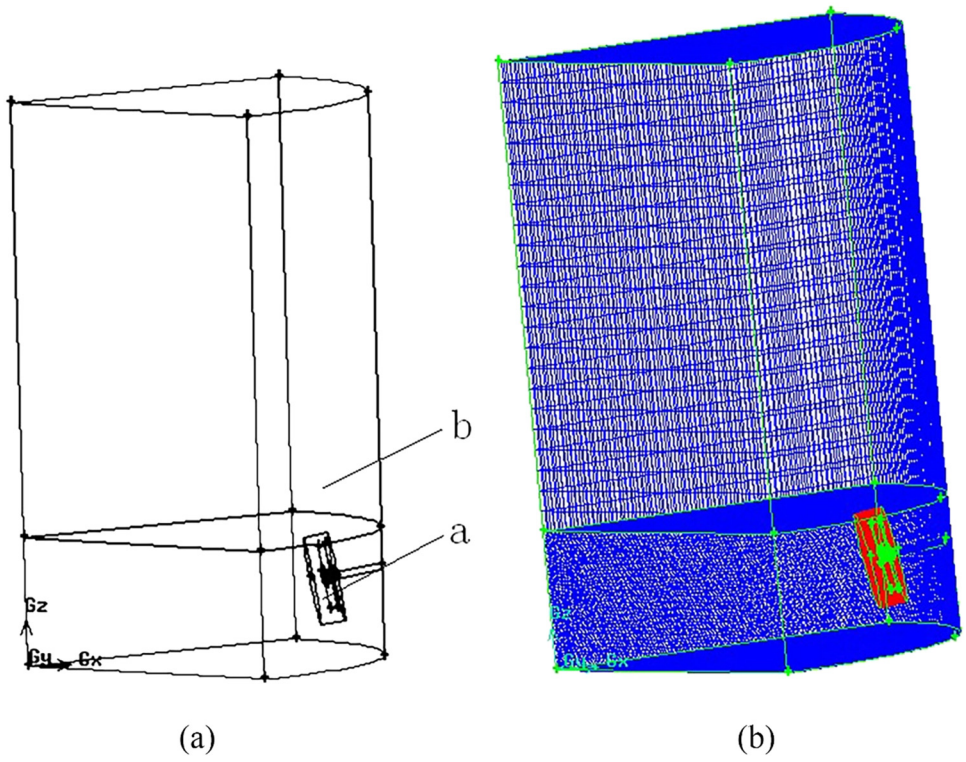

Figure 4: Computational domain structure diagram (a) and meshes of the symmetric model (b).

the geometry. The method of combining unstructured grids of different sizes was used to divide the rotating part of the blade and the static part at the bottom of the stirring tank into grids, respectively. The rotating part of the blade adopted a relatively fine tetrahedral grid, while the stationary part at the bottom of the stirred tank adopted a slightly larger tetrahedral grid. The rotating part of the blade, agitator shaft, and the stationary part at the bottom of stirring tank were meshed encrypted to increase the calculation accuracy. The total number of grids was about 970,000, and the distribution of grid nodes is shown in Figure 4(b).

2.4 Numerical calculation method of side-entering stirring device

Fluent software was used to simulate the two-phase flow field in the stirring tank. The multi-reference frame (MRF) method was used to deal with the interaction between the moving blade and the stationary slot wall. The rotational coordinate system was adopted for the blade and its nearby fluid region, and the stationary coordinate system was adopted for other regions. The momentum and energy exchange in the two different regions were realized through the interface conversion. The steady-state implicit separation algorithm was used in the solution process.

The fluid in the moving region (*i.e.*, blade region) was set to rotate at the same speed as the stirring blade due to the MRF method used for simulation, while the fluid in the stationary region (*i.e.*, other regions in the tank) was static. The wall of stirring tank was defined as the boundary condition of static wall, while the agitator shaft and agitator paddle were defined as the boundary condition of moving wall. The stirring shaft was in the static fluid region and moved relative to the fluid in the region, the paddle was in the moving fluid region and moved at the same speed as the surrounding fluid, so it was stationary with respect to the fluid in the region. Because the agitator blades were far from the free liquid surface, there is almost no liquid movement at the free liquid surface. Therefore, the free liquid surface can be defined as a symmetric boundary condition, so as to ignore its influence on the whole mixing process. The rotating periodic boundary without pressure drop was used for a pair of quarter cross-sections divided in the tank body, while the interface between the blade area and other areas in the tank was defined as Interface after the surface was bonded in the grid division module.

The finite volume method was used for calculation, the delay modified QUICK difference was used to discrete

the continuous phase, and the second-order upwind difference scheme was used for the diffusion phase. The pressure relaxation factor was set as 0.3, the momentum relaxation factor as 0.7, the kinetic energy relaxation factor as 0.8, and the dissipation rate relaxation factor as 0.8. SIMPLE algorithm was used for pressure–velocity coupling. Due to the use of unstructured grid, a second-order upwind difference scheme was used to improve the calculation accuracy.

3 Analysis of numerical simulation results of side-entering agitator

3.1 Analysis of macro-flow field simulation results

From the simulated flow field distribution, it can be seen that the high-speed zone of liquid flow was mainly concentrated near the agitator blade and the banded region formed below it, and the maximum velocity appeared near the agitator blade end, which was 10 m/s. The velocity near the blade area was large and decreased rapidly with the increase of the distance from the blade area. Figures 5 and 6 show the simulated macroscopic velocity fields in different planes. As shown in Figure 5, the rotating impeller produced an axial flow with a certain downward angle, which flowed to the center of the tank. Part of the fluid turned to flow along the tank bottom to the tank center after hitting the tank bottom. Because four agitators were evenly arranged in the tank, the four streams of fluid collided with each other in the center of the tank and formed a strong axial liquid flow, rising up to the liquid surface. Then they turned into a radial flow to the tank wall, and flowed down to the bottom of the tank along the tank wall, forming an obvious up and down circulating flow in the tank.

The horizontal cross-section flow field at the axial height $z = 1.4$ m is shown in Figure 6. Due to the 7° inclination angle to the right when the agitator was arranged, the axial flow generated by the four blades formed a counterclockwise circular flow around the tank axis on the horizontal plane. The flow in the center of the tank was mainly upward along the axial direction of the stirring tank, so the horizontal flow was not obvious. A small vortex in a clockwise direction was formed near the wall

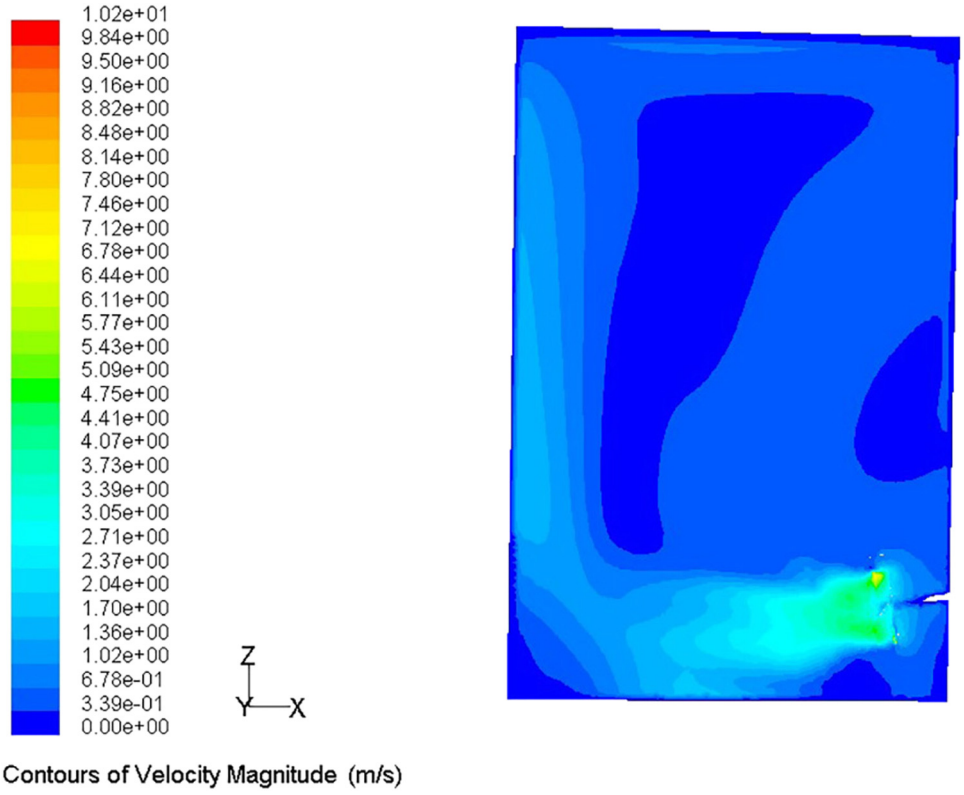

Figure 5: Velocity cloud in $y = 0$ plane.

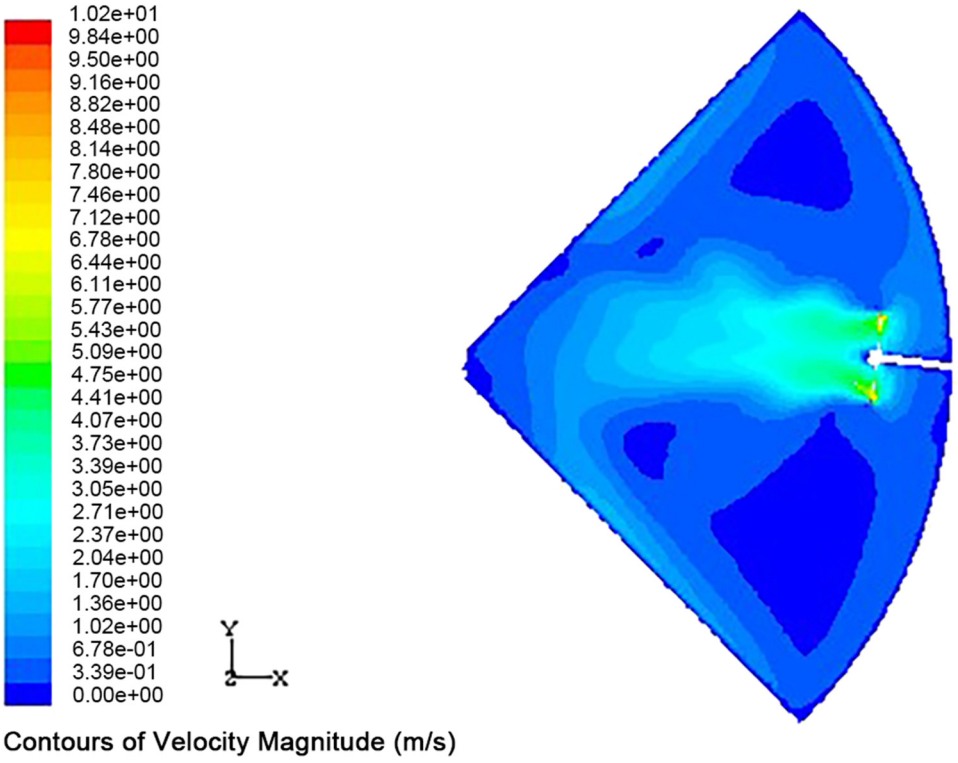

Figure 6: Velocity cloud in plane $z = 1.4$.

of the tank between each two blades, which was generated by the partial liquid flow outside the large circulation under the action of the adsorption force at the rear end of the blade. The flow pattern of the upper part of the tank was relatively simple, and the flow field was like a fountain. The fluid in the center of the tank flowed upward from the bottom of the tank to the liquid surface, while the fluid around the tank flowed down from the liquid surface to the bottom of the tank. The fluid flow velocity in the center of the tank was slightly larger than that in the surrounding tank wall, but the horizontal flow velocity was relatively slow overall after reaching a certain height, and the velocity was about 0.2–0.4 m/s.

3.2 Velocity distribution on the central axis of the stirring tank

The fluid velocity components in the stirring tank included axial velocity, radial velocity, and tangential velocity. In this article, the speed direction was specified as follows: the reference coordinate system was established with the center of the circle at the bottom of the stirring tank as the origin. The radial velocity was positive in the positive direction of the *X*-axis, and negative in the opposite direction. The axial velocity was positive in the positive direction of the *Z*-axis, and negative in the opposite direction. Tangential velocity was positive in the positive direction of the *Y*-axis, and negative in the opposite direction. Figure 7 shows the combined velocity on the central axis of the stirring tank and the distribution of each velocity component. It can be seen from the figure that the main velocity on the central axis of the stirring tank was axial velocity, and its change trend was consistent with that of the combined velocity. The axial velocity increased from the bottom of the stirring tank with the increase in the height of liquid level, and reached the maximum value about 2 m from the bottom, then gradually decreased to 0 at the liquid level. There was a certain tangential velocity component near the center of the tank bottom, but it decreased rapidly with the increase of z value, indicating that there was vortex in the fluid near the center of the tank bottom, which was caused by the large cycle formed in the lower part of the tank.

3.3 Velocity distribution in the vertical plane of the stirring tank

The purpose of stirring is to make the material have speed, so the stirring effect was evaluated by analyzing

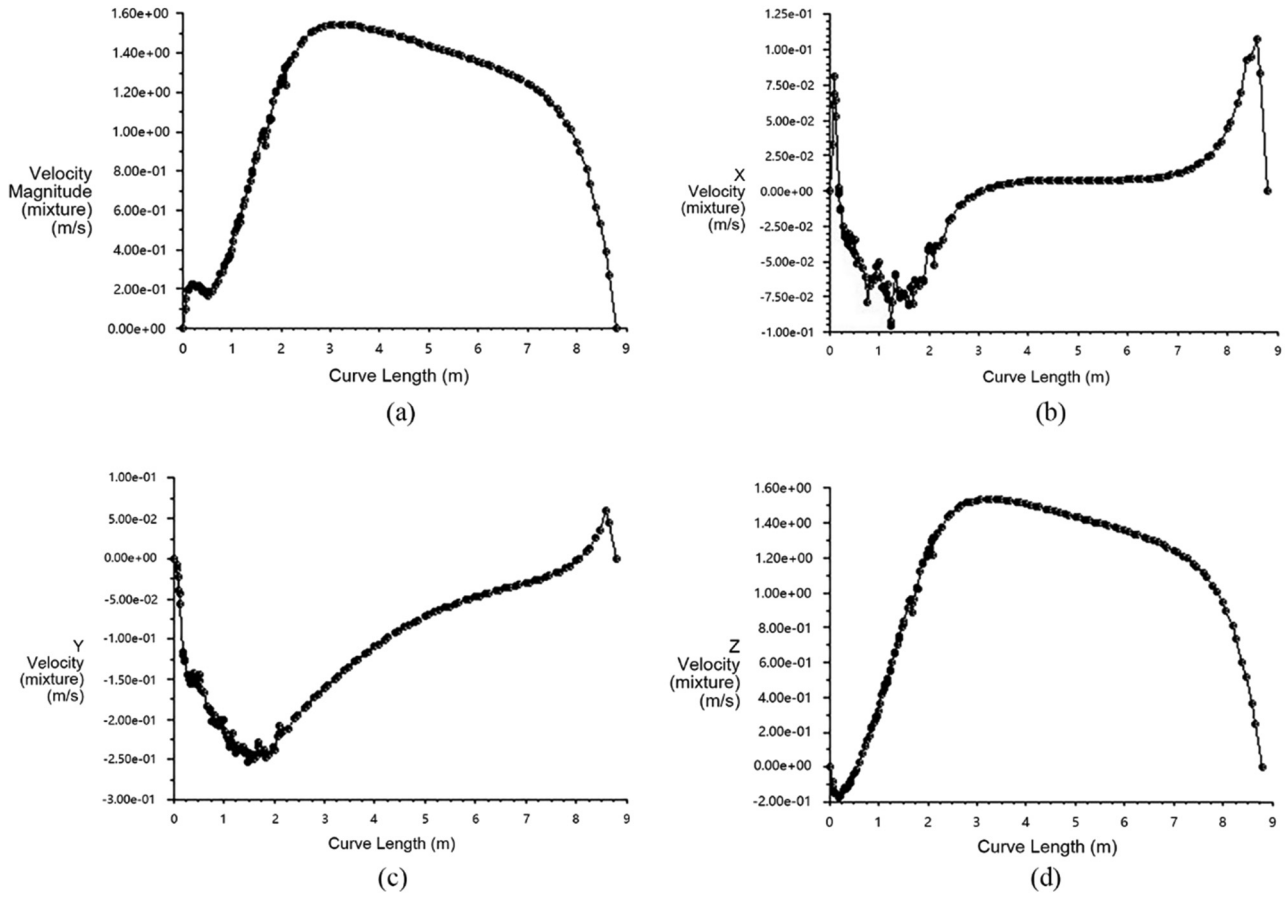

Figure 7: Velocity distribution of the center axis of the stirring tank. (a) Velocity distribution on the central axis, (b) radial velocity distribution along the central axis, (c) tangential velocity distribution on the central axis, and (d) axial velocity distribution along the central axis.

the velocity distribution of the material flow field. Different x and z values were taken in the $y = 0$ plane to analyze the axial and radial velocity distributions, respectively. In the bottom and middle of the stirring tank where the flow field velocity changed sharply, the value interval was small. In the part where the flow field changed slightly, the value interval was large. The values of x were 0.3, 2.0, 3.5, and 5.0 m, and the values of z were 0.5, 1.5, 4.0, and 8.5 m. The axial velocity distribution in the plane $y = 0$ is shown in Figure 8, and the radial velocity distribution is shown in Figure 9.

It can be seen from Figure 8 that the range that fluid flow velocity changed largely and was mainly concentrated at the bottom of the stirring tank to 2–3 m away from the bottom, and the change trend was consistent. The velocity near the tank wall increased sharply at first, and then decreased after maintaining a section of high-speed zone. This kind of distribution was mainly caused by the axial flow with a certain downward inclination angle generated by the rotation of the stirring blade, which rushed to the bottom of the stirring tank and then developed in the radial negative direction of the stirring tank. The fluid velocity in the middle section of the stirring tank changed little, and it increased slightly near the liquid level. With the increase of x value, the flow velocity at the bottom of the stirring tank increased until it reached the maximum near the end of stirring blade. However, the flow velocity decreased gradually with the increase of x value from the middle of the stirring tank to the liquid level and increased slightly near the wall. The velocity near the axis of the stirring tank changed gently, which indicated that the fluid developed toward the liquid level after interacting with the other three axial flows in the center of the stirring tank and then flowed toward the wall of the stirring tank after passing through the liquid level. The fluid distribution presented a "fountain shape." A circulating flow was formed on the vertical surface of the fluid stirring tank to achieve the purpose of stirring.

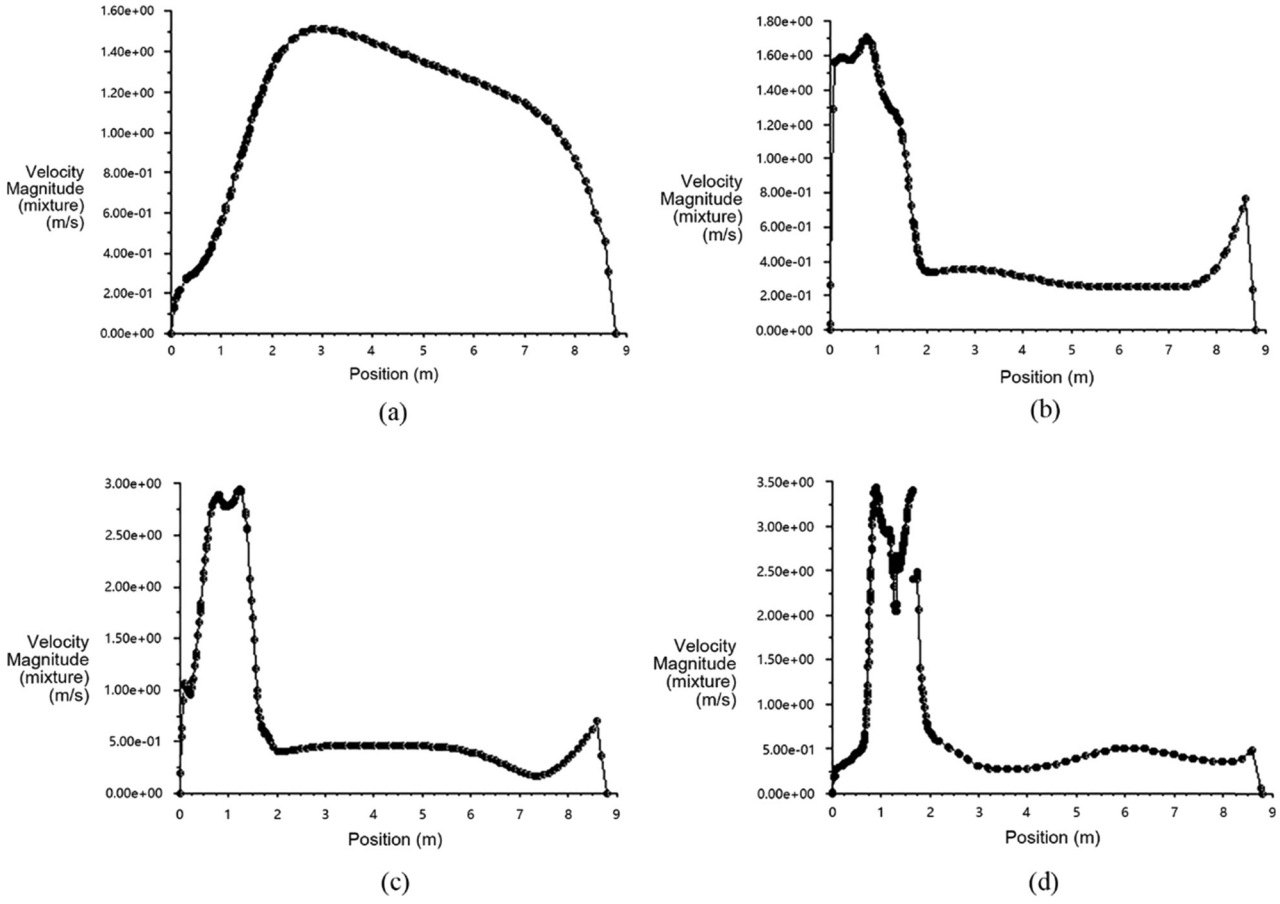

Figure 8: Axial velocity distribution in the plane of straight line $y = 0$. (a) Axial velocity distribution on the line $x = 0.3$ m, (b) axial velocity distribution on the line $x = 2.0$ m, (c) axial velocity distribution on the line $x = 3.5$ m, and (d) axial velocity distribution on the line $x = 5.0$ m.

It can be seen from Figure 9 that at the bottom of the stirring tank, the axial velocity of the fluid increased sharply due to the rotation of the stirring blades. As the fluid flowed toward the center of the stirring tank, the axial velocity changed slightly when it decreased to a certain value, especially in the high-speed axial flow area, which also proved that the agitator blade mainly generated axial flow. The fluid in the middle of the stirring tank flowed upward in the center of the stirring tank and downward around the tank wall, and the flow velocity in the center of the stirring tank was greater than the flow velocity near the tank wall. The flow velocity from the tank wall to the center of the stirring tank decreased first and then increased. The fluid formed a cycle with high peripheral flow velocity and low internal flow velocity. The axial velocity near the liquid level changed little and the fluid near the liquid level was mainly a radial flow from the center of the stirring tank to the tank wall.

3.4 Gas phase distribution in stirring tank

Through the intermediate transition reaction of oxygen and sulfite in the flue gas, part of the calcium sulfite is converted to gypsum, which is chemically called calcium sulfate dihydrate. The remaining calcium sulfite in the slurry of the absorption tower is oxidized by the air pumped in by the oxidation fan to produce calcium sulfate. The reaction process is mainly completed by the reaction of hydrogen sulfite and oxygen. The second purpose of agitation is to enhance the diffusion of oxidized air, promote the oxidation of calcium sulfite, the growth of gypsum crystals, and the dissolution of limestone. Therefore, the more evenly the air diffuses, the better the oxidation reaction will be. The ventilation device was located 1.4 m away from the bottom of the stirring tank, placed 1.8 m away from the tank wall horizontally, with a diameter of 200 mm and a ventilation speed of

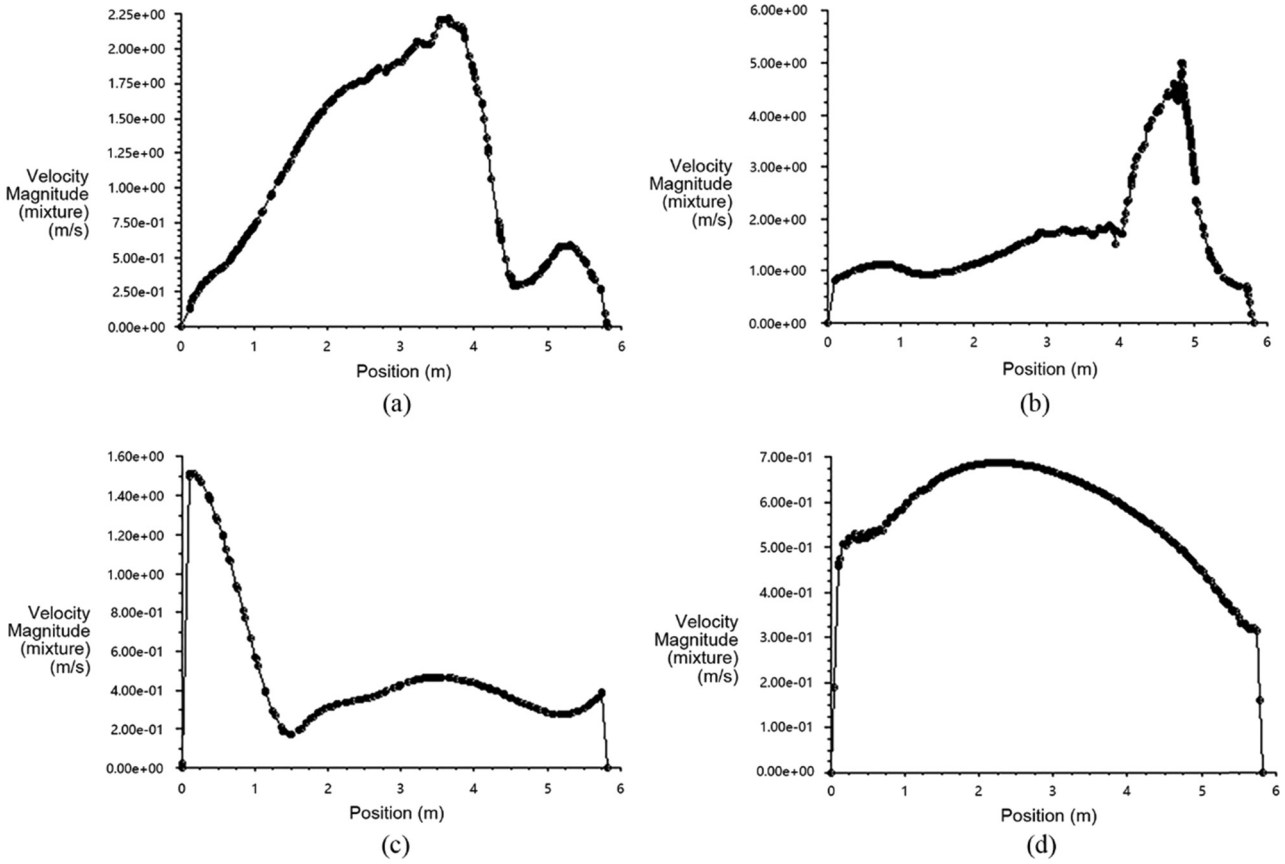

Figure 9: Radial velocity distribution in the plane of straight line $y = 0$. (a) Radial velocity distribution on the line $z = 0.5$ m, (b) radial velocity distribution on the line $z = 1.5$ m, (c) radial velocity distribution on the line $z = 4.0$ m, and (d) radial velocity distribution on the line $z = 8.5$ m.

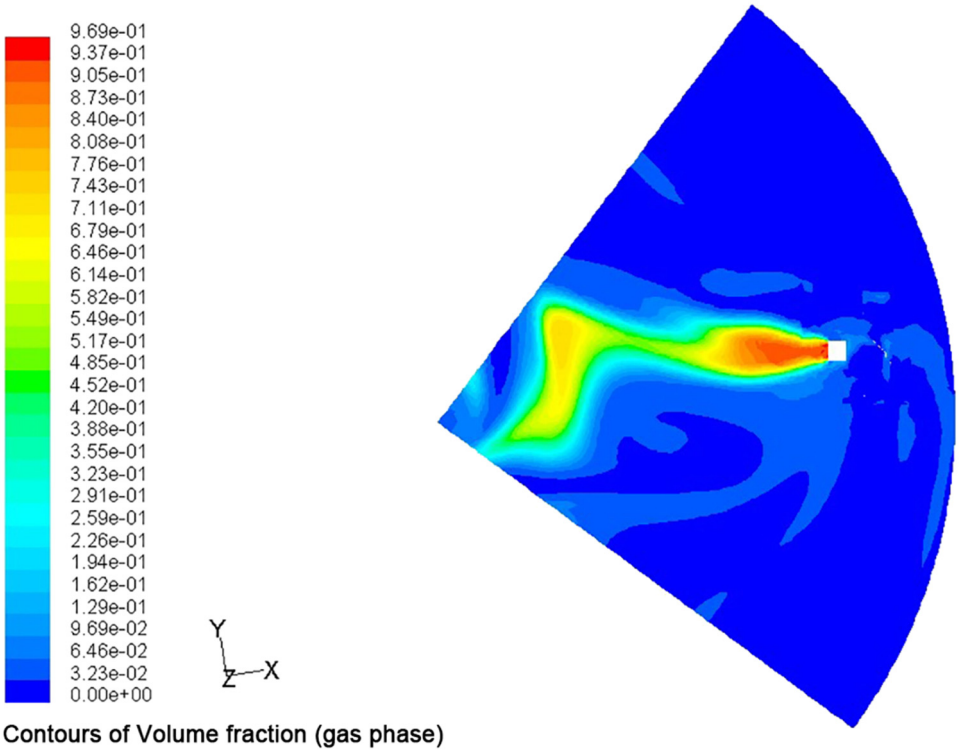

Figure 10: Gas volume distribution in horizontal plane $z = 1.4$ m.

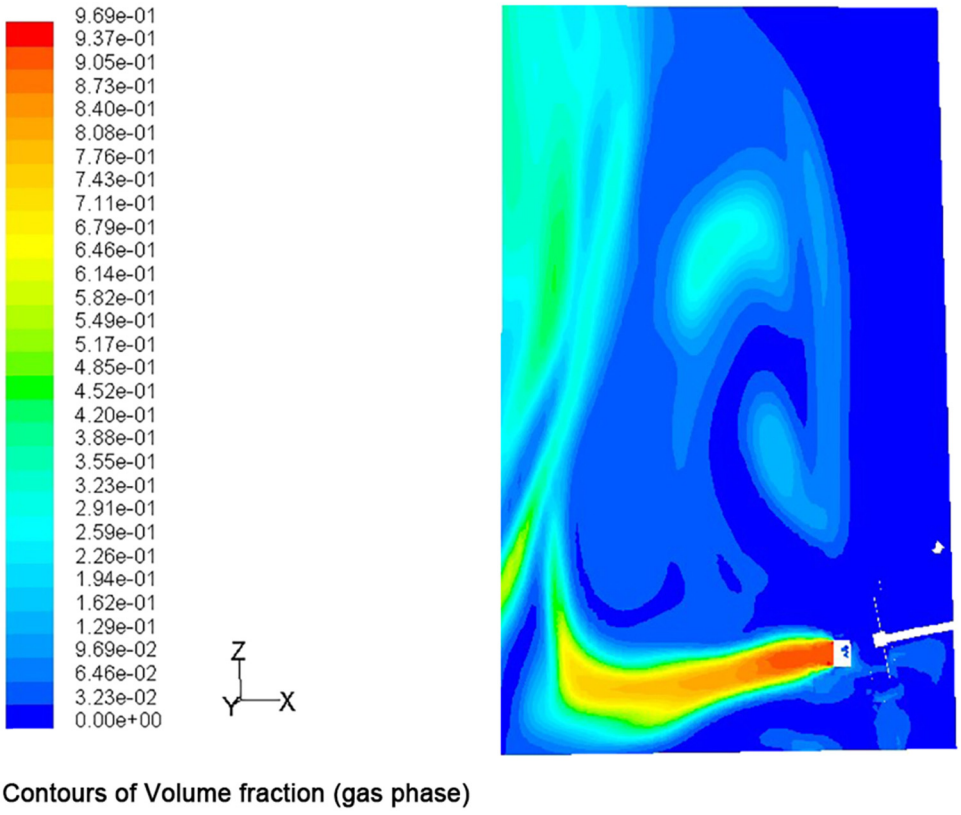

Figure 11: Vertical plane gas volume distribution.

7 m/s. The volume distribution of gas phase on the horizontal plane of the stirring tank z = 1.4 m is shown in Figure 10, and the volume distribution of gas phase on the vertical plane is shown in Figure 11.

It can be seen from Figures 10 and 11 that the oxidized air flowed to the bottom of the stirring tank together with the fluid under the action of axial flow with a certain downward inclination angle after being ejected from the nozzle. It flowed upward after collision with the bottom of the stirring tank. At this time, it collided with other fluid flowing to the center of the stirring tank again. Part of the oxidized air moved upward along the central axis of the stirring tank under the dual action of buoyancy and fluid, and part of the oxidized air changed direction on the horizontal plane to form a bottom circulation. The oxidized air speed decreased gradually when it flowed from the nozzle to the center of the stirring tank, and part of the energy was transferred to the surrounding fluid, which plays a stirring effect at the same time. After the oxidation air collided in the center of the stirred tank, it flowed to the liquid surface and diffused along the center of the stirred tank to the tank wall after obtaining a radial velocity.

4 Conclusion

In this article, numerical simulation was carried out on the side-entering agitator used in desulfurization tower of power plant. The flow field distribution obtained from simulation shows that the high-speed zone of liquid flow is mainly concentrated near the agitator blade and the belt region formed below it, and the maximum flow rate is near the end of the agitator blade, which is 10 m/s. The four streams of fluid generated by the four stirring blades collide with each other in the center of the tank and form a strong axial liquid flow, which rises up to the liquid level, then turns into a radial flow to the wall of the surrounding tank, and flows down to the bottom of the tank along the wall. An obvious “fountain” up and down circulating flow is formed in the tank body to achieve the purpose of stirring. The intense agitation is beneficial to the formation of grain, improve the utilization rate of oxygen, and promote the mixing of slurry and prevent scaling.

Funding information: The authors acknowledge the support of the National Natural Science Foundation of China (No. 52176040, 52006126).

Author contributions: All authors have accepted responsibility for the entire content of this manuscript and approved its submission.

Conflict of interest: The authors state no conflict of interest.

Data availability statement: The data that support the findings of this study are available from the corresponding author upon reasonable request.

References

[1] Liu HZ, Guo YX. Comprehensive discussion on control technology of sulfur dioxide pollution from coal burning in China. Energy Environ Prot. 2005;19(1):13–4.

[2] Hao YR, Meng C, Liu KK. Analysis on the development of industrial air pollution control technology. China Resour Compr Util. 2020;38(6):132–4.

[3] Sai JC, Wu SH, Wang HT, Qin YK. Present situation of Chinese FGD technology and localization of manufacture issue. Power Syst Eng. 2003;19(1):53–4.

[4] Hao JM, Wang SX, Lu YQ. Technical manual of sulfur dioxide pollution control from coal burning. Beijing: Chemical Industry Press; 2001.

[5] Cai XJ, Wu LZ. The construct of side-inserted stirrer. Petro-Chem Eq. 2001;30(B05):45–6.

[6] National Chemical Equipment Design Technology Center Station Mixing Engineering Technology Committee. Mixing equipment. Beijing: Chemical Industry Press; 2019.

[7] Gómez C, Bennington CPJ, Taghipour F. Investigation of the flow field in a rectangular vessel equipped with a side-entering agitator. J Fluid Eng – Trans ASME. 2010;132(5):051106.

[8] Havryliv R, Kostiv I, Maystruk V. Using the computational fluid dynamic software to mixing process modeling in the industrial scale vessel with side-mounted agitator. 2020 10th International Conference on Advanced Computer Information Technologies (ACIT). Deggendorf, Germany: IEEE; 2020. p. 192–5.

[9] Fathonah NN, Madhania S, Nurtono T, Winardi S. Simulation of scale-up criteria for side-entry stirred tank in laboratory scale. IOP Conference Series: Materials Science and Engineering. Vol. 1053. Issue 1; 2021. p. 012106.

[10] Fathonah NN, Nurtono T, Kusdianto K, Madhania S, Wahyudiono W, Winardi S. Numerical study of the hydrodynamic characteristics in an agitated tank with side-entry mixer: the effect of stirrer entry angle. Int J Technol. 2019;10(3):521–30.

[11] Al-Kouz W, Bendrer BAI, Aissa A, Almuhtady A, Jamshed W, Nisar KS, et al. Galerkin finite element analysis of magneto two-phase nanofluid flowing in double wavy enclosure comprehending an adiabatic rotating cylinder. Sci Rep-UK. 2021;11(1):1–15.

[12] Manzoor R, Khalid A, Khan I, Islam SU, Baleanu D, Nisear KS. Numerical simulation of drag reduction on a square rod detached with two control rods at various gap spacing *via* lattice Boltzmann method. Symmetry. 2020;12(3):475.

[13] Kehn RO. Comparing top entry *versus* side entry agitator performance in low viscosity blending. Can J Chem Eng. 2011;89(5):1059–67.

[14] Grenville RK, Giacomelli JJ, VanOmmeren GJ, Hastings CF, Walters MJ. Blending in above ground storage tanks with side-entering agitators. Chem Eng Res Des. 2018;137:395–402.

[15] Wesselingh JA. Mixing of liquids in cylindrical storage tanks with side-entering propellers. Chem Eng Sci. 1975;30(8):973–81.

[16] Fang J, Sang ZF, Yang BQ. Numerical simulation of three-dimensional flow field in side entry agitator. Petro Mach. 2009;37(1):30–4.

[17] Chen ZP, Zhang XW, Lin XH. Design and selection manual of stirring and mixing equipment. Beijing: Chemical Industry Press; 2004. p. 141–2

[18] Lahey RT, Drew DA. On the development of multidimensional two-fluid models for vapor/liquid two-phase flows. Chem Eng Commun. 1992;118:125–39.

[19] Drew DA. Mathematical modeling of two-phase flow. Annu Rev Fluid Mech. 1983;15:261–91.

[20] Hua JS, Wang CH. Numerical simulation of bubble driven liquid flows. Chem Eng Sci. 2000;55(19):4159–73.

[21] Wang JJ, Li LC, Gu XP, Feng LF. Progress on CFD simulation of gas–liquid two-phase flow in stirred tank reactor. Process Equip Pip. 2012;49(1):1–4.

[22] Chen J, Xiao WD. Gas–liquid flow dynamics simulation in side-entering stirred tank. CIESC J. 2013;64(7):2344–52.

[23] Song YL. Numerical simulation of gas–liquid two-phase flow in multi-layer paddle stirring tank. M.Sc. thesis. Beijing, China: Beijing University of Chemical Technology; 2006.

[24] Wang FJ. Computational fluid dynamics analysis principle and application of CFD software. Beijing: Tsinghua University Press; 2004.

[25] Launder BE, Spalding DB. Lectures in mathematical models of turbulence. London: Academic Press; 1972.